Eur. J. Mech. B - Fluids 19 (2000) 765–788

S0997-7546(00)00115-1/FLA

Numerical simulation (DNS and LES) of manipulated turbulent boundary layer flow over a surface-mounted fence

Alexander Orellano, Hans Wengle *

Institut für Strömungsmechanik u. Aerodynamik, LRT/WE 7, Universität der Bundeswehr München, 85577 Neubiberg, Germany

(Received 7 April 1999; revised 3 November 1999; accepted 14 December 1999)

Abstract – Results from numerical simulations are presented for manipulated turbulent boundary layer flow over a surface-mounted fence, for a Reynolds number of $Re_h = 3000$ (based on fence height, h, and maximum inflow velocity, U_∞). First, a reference data set was provided from a Direct Numerical Simulation (DNS) using 51.6 million grid points to resolve all the relevant spatial scales of the flow. A Large-Eddy Simulation (LES), using 1.67 million grid points, was validated with this reference solution and compared with experimental data for the same Reynolds number. Then, manipulated flow cases were investigated applying time-periodic forcing through a narrow slot upstream of the flow obstacle. High-frequency forcing, with $Str_1 = f_1 h/U_\infty = 0.60$, leads to about 10% reduction of the mean re-attachment length. A much stronger reduction of about 36% could be achieved by low-frequency forcing with $Str_2 = f_2 h/U_\infty = 0.08$. In the latter case, large-scale coherent structures are created between the location of the disturbance and the fence, they roll over the flow obstacle (nearly unaffected) and in rolling downstream they still grow in size until they fill out the entire height of the separation zone behind the fence. In agreement with corresponding experiments of Siller and Fernholz in 1997 for a higher Reynolds number ($Re_h = 10500$) the optimum forcing Strouhal number seems to be related to the low-frequency movement of the entire separation bubble and not to the instability mode of the separating shear layer.©2000 Éditions scientifiques et médicales Elsevier SAS © 2000 Éditions scientifiques et médicales Elsevier SAS

turbulent flow over a fence / time-periodic forcing / optimal frequency / control of mean re-attachment length / direct and large-eddy simulation

1. Introduction

It has been demonstrated in the literature that the structure of turbulence can be forced to attain a certain desired behaviour of the flow, such as drag reduction, minimization/maximization of mixing, or the reduction of a separation zone. To do this properly and efficiently a deeper understanding of the underlying dynamics of the organized (coherent) structures in turbulent flows is required. The basic idea is to control the flow by interacting with these structures. Information about the three-dimensional and time-dependent flow fields can be obtained from measurements in the real world of the laboratory or, thanks to the increased power of modern 'super'-computers, from numerical simulations of idealized flow situations.

In this paper we present results from numerical simulations of manipulated turbulent boundary layer flow over a surface-mounted fence. In general, there are two basic numerical simulation concepts available to calculate the three-dimensional and time-dependent structure of a turbulent flow (based on the solution of the Navier–Stokes equations). The Direct Numerical Simulation (DNS) resolves all the relevant scales in a turbulent flow, but its range of application is limited to relatively small Reynolds numbers (often too small from a practical engineering point of view). Moin and Mahesh [1] illustrate the complementary nature of experiment and direct numerical simulation in turbulence research. Significant insight into the turbulence physics has been gained from DNS of certain idealized flows that cannot be easily attained in the laboratory. Large-Eddy

* Correspondence and reprints; e-mail: hans.wengle@unibw-muenchen.de

Simulation (LES) delivers directly the spatial and temporal behaviour of at least the large-scale structures also at higher Reynolds number, and only the effects of the small-scale motions which cannot be resolved on a given computational mesh need to be modelled with a so-called sub-grid scale model. The strategy which we applied in this work is to solve the flow problem first at a low Reynolds number with DNS and then use the result as a reference for a LES carried out with a significantly smaller number of grid points. After having validated the LES in comparison with the DNS result and with available experimental data we used the LES concept to carry out the numerical simulations for the manipulated flow cases. With the experience gained at low Reynolds number it will be possible to apply the LES concept to non-manipulated and manipulated flow cases at higher Reynolds number. To further validate the LES results for higher Reynolds numbers, a comparison with corresponding experimental data is desirable (at least for a non-manipulated flow case).

The purpose of the work described in this paper is to reduce the length of the downstream extension of the separation zone behind a surface-mounted flow obstacle. Depending on the angle between the mean flow vector at the separation point and the mean inflow direction different mean re-attachment lengths are created. For example, the backward-facing step flow exhibits a mean recirculation length of about 6.5 step heights, h (for a step height Reynolds number of $Re_h \approx 3000$), the fence flow creates a larger mean re-attachment length of about 13 fence heights (for the same Reynolds number) and a still longer reverse-flow region of at least 17 fence heights (at $Re_h = 14000$) is known to be created behind a vertical plate (a double fence with height $2h$) with a long splitter plate in the plane of symmetry.

A review of research on turbulent flow re-attachment was given by Eaton and Johnston [2] and a more recent one by Adams and Johnston [3,4]. Reviews on transitional, turbulent and perturbed free shear layers were presented by Ho and Huerre [5] and by Liu [6]. Reviews on the management and control of laminar/turbulent flows were given by Bushnell and McGinley [7], Fiedler and Fernholz [8], Gad-el-Hak [9], Lumley and Blossey [10], and a most recent collection of review articles by Gad-el-Hak et al. [11].

For turbulent flow over a backward-facing step (with turbulent boundary layer inflow) a DNS is available from Le, Moin and Kim [12], and a corresponding LES from Akselvoll and Moin [13] (for a step height Reynolds number of 5100). Their results are compared with experimental data of Jovic and Driver [14]. The manipulation of the free shear layer after a backward-facing step was investigated by Hasan [15] for laminar separation ($Re = 11000$) and by Hasan and Khan [16] for transitional and turbulent boundary layer inflow ($Re = 15000$ and 30000). Experimental data for a manipulated fully turbulent backward-facing step flow ($Re = 12000$ to $Re = 33000$) was presented in Chun and Sung [17,18]. Results from a manipulated transitional backward-facing step flow ($Re_h = 3000$) have been provided in experimental studies by Huppertz and Janke [19] and, in a joint paper by Wengle et al. [20], these experimental results were compared with DNS results.

Results from experimental studies on turbulent flows over a surface-mounted fence have been presented by Good and Joubert [21] ($Re = 10^6$–10^7) and on flow over a vertical plate with symmetrical splitter plate on the downstream side by Ruderich and Fernholz [22] and by Castro and Haque [23] ($Re_h \approx 14000$). Kelso et al. [24] report on manipulated flow over a fence ($Re_h = 26000$) and Miau et al. [25] used a vertically oscillating fence upstream of the edge of a backward-facing step to reduce the mean recirculation length.

Related to the topic of this paper are also reports on more recent experimental work by Kiya et al. [26], by Sigurdson [27] ($Re_d \approx 10^5$) and by Weickgenannt and Monkewitz [28] on a forced recirculation bubble on a blunt cylinder aligned coaxially with the free stream.

In a flow case with a re-attaching shear layer bounding a separation region behind a flow obstacle there are two different instabilities involved: the Kelvin–Helmholtz instability of the free shear layer and a ‘shedding’-type instability of the entire separation bubble. The term ‘shedding’-type instability has been created by Sigurdson [27] in analogy to the Kàrmàn vortex shedding in the wake of a transverse cylinder. For a number of different flow cases the ‘shedding’ Strouhal number (based on the maximum height of the separation zone

behind a flow obstacle) was evaluated in [27] and had the same value, $Str = 0.08$, for all cases. In cases with an incoming boundary layer, the dimensionless frequency of the natural roll-up of the separated shear layer, based on the momentum thickness, θ, at the location of separation, gives another 'universal' Strouhal number, from $Str_\theta = 0.010$ to 0.012, characterizing the shear layer instability mode.

In our case the purpose of the control of the flow is to reduce the size of the separation zone behind the flow obstacle. Then, there is an optimum forcing frequency for a maximum reduction of the mean re-attachment length. In the case of the manipulated backward-facing step flow [20] we used the optimum disturbance frequency found by Huppertz and Janke [19] in a series of experiments, and the optimum forcing Strouhal number ($Str_h = 0.45$, $Str_\theta = 0.012$) is related to the shear layer instability mode and not to the 'shedding'-type mode. In the present paper we investigate the case of turbulent boundary layer flow over a fence, manipulated by time-periodic blowing/suction disturbances in front of the flow obstacle. For the corresponding non-manipulated flow experimental results are available from Larsen [29] ($Re_h = 3000$) and from Siller and Fernholz [30,31] ($Re_h = 10500$).

The main objectives of this study are:

- to provide a DNS reference data base for the non-manipulated flow over a surface-mounted fence at a low Reynolds number ($Re_h = 3000$),
- to validate large-eddy simulations for the non-manipulated flow at low and higher Reynolds number ($Re_h = 3000$, $Re_h = 10500$), and
- to carry out large-eddy simulations (at $Re_h = 3000$) for manipulated flow cases, applying a high-frequency forcing Strouhal number (related to the shear layer mode) and a low-frequency forcing Strouhal number (related to the 'shedding' mode).

In the following section 2 we present the numerical method and the computing strategy used in this study. In section 3 we compare results from different numerical simulations (LES, DNS) and also compare available experimental data with corresponding computational results. In section 4 we present our conclusions.

2. Numerical simulation

2.1. Solution strategies and numerical solution method

2.1.1. Direct Numerical Simulation (DNS)

For a DNS the conservation equations for mass and momentum must be solved without any additional assumptions or modelling related to the effects of the turbulent motion, i.e. the original Navier–Stokes equations must be discretized in space and time such that all the relevant scales in a turbulent flow are resolved. For example, referring to spatial scales, the size of the computational domain must be large enough to accommodate the largest turbulent scales, and the grid spacing must be sufficiently small to enable a resolution of the order of the dissipation length scale, $\eta = (\nu^3/\epsilon)^{1/4}$. Here, ν is the kinematic viscosity of the fluid and ϵ is the dissipation rate in the flow field. Less stringent estimations consider, for example, two-point correlations and energy spectra to judge whether adequate resolution can be achieved.

2.1.2. Large-eddy simulation (LES)

For a LES the low-pass filtered Navier–Stokes equations are solved, i.e. eddies smaller than the grid spacing are removed and their effect on the resolvable motion is provided by a subgrid-scale (SGS) model. In deriving the resolvable scale equations, see e.g. in Rogallo and Moin [32], the proper choice of a filter and of a filter width is involved (top-hat filter, Gaussian filter) and the result exhibits, in addition to correlations

between SGS quantities, the so-called Leonard terms (involving cross-correlations between SGS quantities and resolved quantities). Finally, in numerically solving these resolvabe scale equations the numerical errors and the modelling errors are involved. For a strict separation of the modelling physics and the numerical errors a large ratio of filter size to mesh resolution is required. This is certainly attractive from a theoretical point of view. However, in solving practical problems with complex geometry and large Reynolds numbers, this would be very costly.

An alternative derivation of the resolvable scale equations has been carried out by Schumann [33] and leads directly to the integral form of the Navier–Stokes equations in which time derivatives of cell-volume averages of velocities are related to differences of cell-surface averaged stress and momentum flux. Finally, the averages are related to their finite-difference operators (second-order method on a staggered computational mesh). We follow this approach and, in this paper, the unknown SGS stresses are related to the GS velocity via an eddy viscosity model, the classical Smagorinsky SGS model (using the empirical constant $c_s = 0.1$). In grid volumes next to rigid walls we use for the mixing length the smaller value of κx_n and $0.1(\Delta x \Delta y \Delta z)^{1/3}$ (where x_n is the distance normal to a wall). From the point of view of filtering approach we use a filter width equal to the grid spacing and the effects of all the unknown terms are modelled all together by this eddy viscosity model which acts as a sink of energy for the short waves in the flow.

More details on the problems involved in LES can be found in the reviews of Rogallo and Moin [32], Ciofalo [34] and Fureby [35].

2.1.3. Numerical solution method

The numerical code used in this paper is based on a finite-volume formulation of the Navier–Stokes equation for an incompressible fluid on a non-equidistant and staggered Cartesian grid. For LES we follow the approach of Schumann [33] in deriving the resolvable scale equations from the integral form of the balance equations. The discretization in space used here is of second-order (central) for the convective and the diffusive terms. For the time advancement of the momentum equations an explicit second-order time step is used (leap-frog with time-lagged diffusion). For example, the u-component at the new time level $n + 1$ is evaluated from

$$u^{n+1} = u^{n-1} + 2\Delta t\left[C\left(u^n\right) + D\left(u^{n-1}\right) - G\left(p^{n+1}\right)\right], \tag{1}$$

where C, D and G represent the discrete convection, diffusion and gradient operators, respectively. The pressure at the new time level, p^{n+1}, is evaluated from solving the discretized Poisson equation

$$\mathrm{Div}\left[G\left(p^{n+1}\right)\right] = \frac{1}{2\Delta t}\mathrm{Div}\left(u^*\right), \tag{2}$$

where u^* is an intermediate velocity field calculated by omitting the pressure gradient in (1). We arrive at the required divergence-free velocity field at the new time level, u^{n+1}, by applying the velocity correction

$$u^{n+1} = u^* - 2\Delta t G\left(P^{n+1}\right). \tag{3}$$

The solution of the Poisson equation can be done either directly or iteratively. The iterative solver used here is the well known point-by-point velocity-pressure iteration described by Hirt et al. [36]. This iterative pressure-velocity correction cycle is stopped as soon as the dimensionless divergence of the (incompressible) flow reaches levels below 10^{-3} at all grid points after every time step. This iterative method has the advantage that it can easily be applied to quite arbitrary geometry of flow obstacles in the computational domain. Its disadvantage is that it is very costly to reach divergence levels down to machine accuracy (which is not required

in our case). Acceleration of the convergence of the iteration cycle is possible by applying smoothing with a multigrid cycle.

In this paper the flow over a flow obstacle with sharp edges is calculated. Central differencing of the convection terms creates spatial oscillations of the solution upstream of the sharp edges and corners. In general, these so-called 'wiggles' signal insufficient spatial resolution of gradients in the flow field, see, e.g., in Gresho and Lee [37], and consequently, they can be removed by using more grid points in the critical flow regimes. This can be achieved by compressing the non-equidistant grid immediately in front of the sharp edges or by applying local grid refinement (which is still the object of current research). This problem can be severe in LES at high Reynolds number. However it is not present in a DNS which per definition should provide sufficient spatio-temporal resolution. Fortunately, the effect of the 'wiggles' on the statistics is limited to a narrow zone upstream of the flow obstacle (see, e.g., the statistics discussed in section 3.2, where the little bumps in the vertical profiles can be seen at about $Z \approx 2.4$), the result outside of this zone of influence upstream of the sharp edge and the flow field downstream is unaffected. The use of low-order upwind methods to damp the 'wiggles' is not recommended because it also dampens the smaller-scale velocity fluctuations.

2.1.4. Validation of the numerical code

In the following we present some published information on the validation of the numerical code used here. First, the code has been applied to 2D and 3D, steady and unsteady benchmark problems of laminar flow over a square cylinder unsymmetrically placed in a plate channel. In Schäfer et al. [38] the results are compared between 17 participants of the 'computing contest'. For fully developed turbulent channel flow ($Re_\tau = 180$) computational results from Manhart [39] for coarse and fine grids and for local grid refinement have been compared with the spectral results of Kim et al. [40]. For the same flow a comparison of results using either a second-order scheme or a fourth-order compact scheme is presented in Meri et al. [41]. The minimal turbulent channel flow unit has been used as a test case for three different codes (including our code), see Manhart et al. [42]. Data for the performance (memory and CPU-time requirements) are presented and the accuracy of the results is measured in comparison with the spectral reference solutions of Jimenez and Moin [43]. Finally, the results of a workshop on turbulent flow past bluff bodies presented by Rodi et al. [44] contain a comparison between different codes (including our code) used to calculate the fully turbulent flow around a surface-mounted cube in plane channel flow for a low Reynolds number ($Re = 3000$). For $Re = 40000$ the performance of the different codes has been measured in comparison with experimental data from Martinuzzi [45].

2.1.5. Computation of the statistics

The direct results from DNS and LES are the time-dependent and three-dimensional velocity and pressure fields. After an initial transient phase of the calculation (not used for collecting samples for the statistics) the mean fields have been obtained by averaging samples in time and by making use of spatial averaging in the homogeneous lateral direction of the flow problem. As soon as the mean fields have reached stable (i.e. time-independent) values, the fluctuating fields can be evaluated. Then, samples for the evaluation of the statistics have been collected over about 90 reference times, $T_{ref} = h/U_\infty$, for the DNS runs, and over at least 900 reference times for the LES runs.

2.2. Flow configuration, computational grid, and boundary conditions

Note that in the following all the variables are presented in dimensionless form, i.e. the velocities and the velocity correlations are made dimensionless with the reference velocity, U_∞, lengths are made dimensionless with the fence height, h.

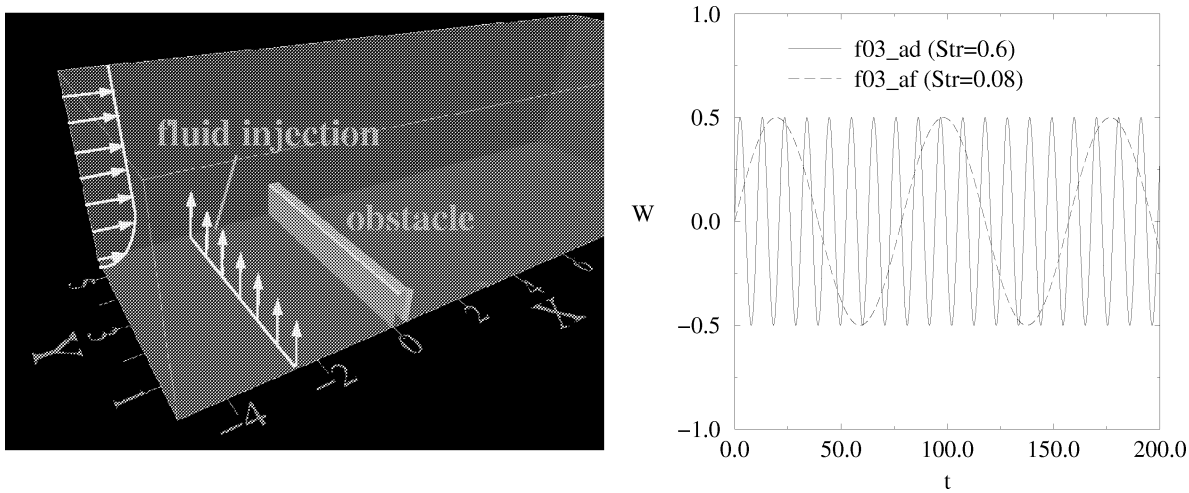

Figure 1. Computational domain with manipulation slot at $X = -3$ (left) and disturbance velocity $W(t)$ (right) at the slot for the two different Strouhal numbers used in the simulations.

2.2.1. Computational domain

The flow configuration selected is a surface-mounted fence with height h, see *figure 1*. In our case, x is the main flow direction (velocity component u), y is the lateral (velocity component v), z is the vertical direction (velocity component w), and $X = x/h = 0$ corresponds to the position of the fence. If all length scales are normalized with the fence height, h, the dimensions of the computational domain are for the reference DNS $(L_x, L_y, L_z) = (39.0, 6.0, 5.0)$ with the inflow cross-section located upstream of the flow obstacle at $X_{inlet} = -16.4$ and for other simulations (coarse grid DNS, LES for $Re_h = 3000$) we have chosen a somewhat shorter domain $(L_x, L_y, L_z) = (32.2, 6.0, 5.0)$ with the inflow cross-section located at $X_{inlet} = -9.6$. For the LES at $Re_h = 10500$ the computational domain was adopted to the experimental conditions, and we used $(L_x, L_y, L_z) = (37.0, 6.0, 6.75)$ with the inflow cross-section located at $X_{inlet} = -15.0$.

2.2.2. Spatial resolution

To resolve the relevant spatial scales of the flow at $Re_h = U_\infty h/\nu = 3000$ we used $(N_x, N_y, N_z) = (896, 192, 300)$ grid points, i.e. a total number of 51.6 million grid points for the reference DNS. For another (coarse grid) DNS we reduced the number of grid points in each direction by about a factor of two, i.e, we used $(N_x, N_y, N_z) = (400, 100, 148)$ which corresponds to a total number of about 6 million grid points. The large-eddy simulations (LES) have been carried out with $(N_x, N_y, N_z) = (236, 96, 74)$, i.e. with 1.67 million grid points for $Re_h = 3000$ and with $(N_x, N_y, N_z) = (400, 96, 150)$, i.e. with 5.76 million grid points for $Re_h = 10500$.

In the homogeneous lateral direction of the flow problem the grid distribution was equidistant. In the other two (X- and Z-) directions we have chosen a non-equidistant grid such that the distance of the first velocity grid point closest to a rigid wall (bottom wall, or obstacle wall) was $\Delta X_{\min} = \Delta Z_{\min} = 0.01$ for the DNS (fine and coarse grid), and for the LES cases we have chosen $\Delta Z_{\min} = 0.02$ and $\Delta X_{\min} = 0.03$, respectively. Measured in units of the viscous length (using the wall shear velocity, u_τ, of the incoming boundary layer) the wall distance of the first velocity grid point was $\Delta Z^+_{\min} \approx 1.5$ for the DNS cases and $\Delta Z^+_{\min} \approx 3.5$ for the LES cases. From an a posteriori evaluation of the local dissipation rate, ϵ, for the fine grid DNS a maximum (dimensionless) dissipation rate of $\epsilon_{\max} \approx 0.25$ has been evaluated (located close to the separation at the leading edge of the flow obstacle). With this value of $\epsilon_{\max}$ the Kolmogorov dissipation length scale could be estimated

from $\eta = (\nu^3/\epsilon)^{1/4}$. Measured in units of this estimated η the spatial resolution of the reference DNS with the fine grid (using 51.6 million grid points) was about $(\Delta X_\eta, \Delta Y_\eta, \Delta Z_\eta) = (2\eta, 6\eta, 3\eta)$.

2.2.3. Boundary conditions

A no slip boundary condition must be used along the rigid walls (i.e. on the bottom wall and on the surfaces of the fence). In our code boundary conditions at rigid walls were specified by assuming that the instantaneous velocity components tangential to the wall, u_P and v_P (at the grid points P closest to the wall) are in phase with the instantaneous wall-shear stress components, τ_{ub} and τ_{vb}. In addition it is assumed that the instantaneous velocity distribution vertical to the wall follows the linear law-of-the-wall, $u^+ = z^+$, for $z^+ \leqslant 11.81$, and a power-law description of the form $u^+ = A(z^+)^B$ (with $A = 8.3$ and $B = 1/7$) is chosen for $z^+ > z_m = 11.81$. Then, the velocity components tangential to a wall (at the grid point next to a wall) can be related to the corresponding wall-shear stress components by integrating the combined instantaneous velocity distributions over the height of the first grid element. With these assumptions the resulting expression can be resolved analytically for the required instantaneous wall-shear stress components, e.g.

$$|\tau_{ub}| = \frac{2\mu|u_P|}{\Delta z} \quad \text{for } |u_P| \leqslant \frac{\mu}{2\rho\Delta z} A^{\frac{2}{1-B}}, \tag{4}$$

$$|\tau_{ub}| = \rho\left[\frac{1-B}{2} A^{\frac{1+B}{1-B}} \left(\frac{\mu}{\rho\Delta z}\right)^{1+B} + \frac{1+B}{A}\left(\frac{\mu}{\rho\Delta z}\right)^{B} |u_P|\right]^{\frac{2}{1+B}} \quad \text{for } |u_P| > \frac{\mu}{2\rho\Delta z} A^{\frac{2}{1-B}}. \tag{5}$$

Here Δz is the vertical width of the grid volume next to a wall, z_m is the upper boundary for the application of the linear law-of-the-wall. In a DNS the linear law-of-the-wall only is required (the viscous sublayer is always resolved). If the viscous sublayer is not resolved in LES, it is common practice in the literature to evaluate the wall-shear stress from a relation of the form $\tau_{ub} = \langle\tau_{ub}\rangle/\langle u_P\rangle u_P$ and to calculate the coefficient of proportionality, $\langle\tau_{ub}\rangle/\langle u_P\rangle$, by using the logarithmic law-of-the-wall. However, using the relation (4) and (5) instead offers the advantage that the ensemble averages $\langle\tau_{ub}\rangle$ and $\langle u_P\rangle$ are not required and the use of the logarithmic law-of-the-wall is avoided.

A slip condition is used along the upper boundary of the computational domain. Periodic boundary conditions are applied in the lateral (homogeneous) direction.

The flow is manipulated by periodic blowing/suction through a narrow cross-wind slot of width $B = 0.1$ located three fence heights upstream (at $X = -3$) of the obstacle. During the experimental investigations of Siller [31] ($Re = 10500$) it became clear that the location of the slot should be outside of the separation zone upstream of the fence (about one fence height) otherwise the vortices produced by the oscillating forcing jet would be caught within this separation bubble. In our unforced case ($Re = 3000$) the mean separation distance was $x_f/h = -2.0$ and we have chosen the slot location at $x/h = -3.0$. The exit velocity of the vertically oscillating control jet, $V_{jet}/U_\infty = w/U_\infty = A \cdot \sin(2\pi f t)$, is realized via a time dependent boundary condition for the vertical (w) velocity at all grid points on a line (at $X = -3$) parallel to the fence (see *figure 1*). In this formulation, A is a dimensionless forcing amplitude.

As an outflow boundary condition, gradients normal to the outflow cross-section of the flow variables have been set to zero and, in addition, a buffer section has been added to the computational domain to avoid possible upstream distortions of the flow by this simple outflow boundary conditions.

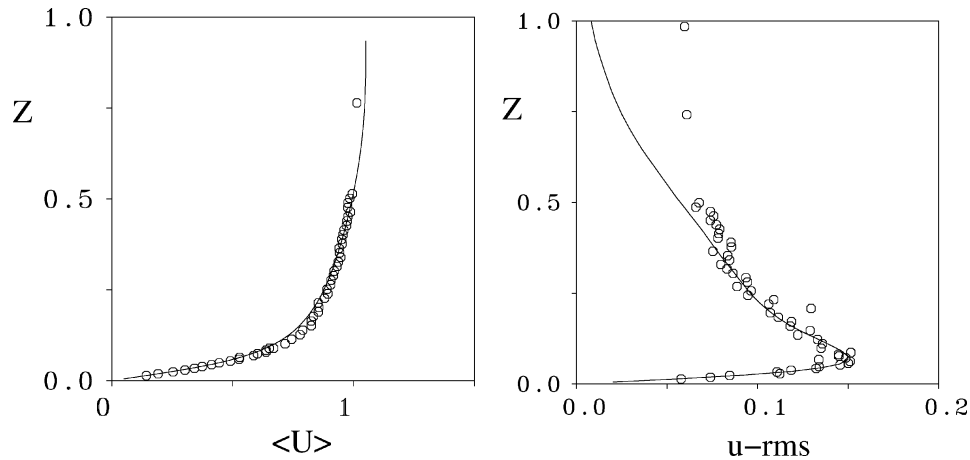

Figure 2. Inflow turbulent boundary layer. Vertical profiles of the mean stream-wise velocity $\langle U \rangle$ (left) and of the rms value of the streamwise velocity fluctuations (right): (full line) DNS, (o) experiment.

2.2.4. Time dependent inflow condition

To create a fully developed turbulent boundary layer we approximated the geometry of a series of vorticity generators located on a cross-wind line immediately after the inlet cross-section (at a distance X_{inlet} upstream of the flow obstacle). Thickness, height and lateral distance of these vorticity generators are the determining parameters for a fast downstream development of the turbulent boundary layer (see in Manhart [46]). The entry length upstream of the flow obstacle is chosen such that at a certain location the desired properties of the turbulent boundary layer are obtained. In our case we tried to create a turbulent boundary layer with $Re_\theta = 240$ as close as possible to the experiment of Larsen [29], see *figure 2*. The only difference between DNS result and the experiment is the large turbulence intensity in the outer region of the turbulent boundary layer created in the wind tunnel. However, we preferred not to have these additional turbulent fluctuations in the outer region of the inflow boundary layer.

2.3. Choice of forcing frequency and amplitude

Two forcing frequencies have been selected to influence, in the first case, the shear layer during its roll-up and pairing phase and, in the second case, the behaviour of the entire recirculation zone. From the large-eddy simulation of the non-manipulated case a first impression of the dominant length-scales and time-scales involved can be obtained from iso-lines of the pressure fluctuations in a vertical cross-section, see *figure 3*, from corresponding videos and from time-records (and its Fourier transforms) at selected locations in the flow field.

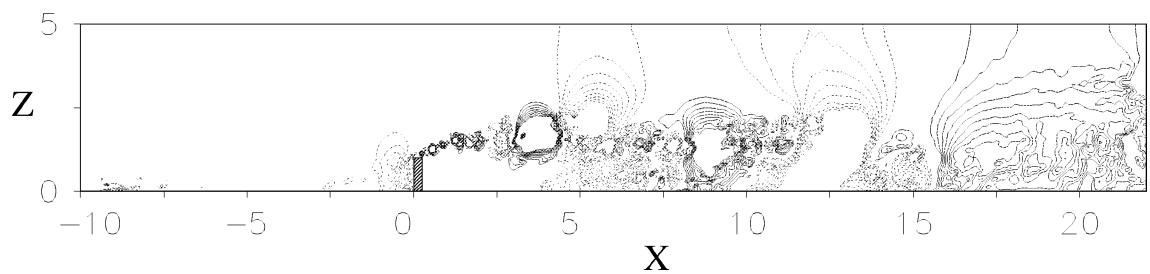

Figure 3. Iso-lines of equal values of pressure fluctuations in a vertical cross-section; (full lines) positive values, (dashed lines) negative values.

Figure 3 clearly shows the first large-scale structures in the shear layer around $X \approx 1.0$, a longer phase with a pairing process up to $X \approx 2.5$ and very large structures in the re-attachment zone around $X \approx 12.5$. From observing the temporal behaviour of a typical structure between X=1.0 and $X \approx 2.5$ and at $X \approx 12.5$ we could estimate their typical frequencies. From this we finally selected a high-frequency forcing Strouhal number, $Str_1 = f_1 h/U_\infty = 0.6$ (to influence the spatially elongated phase of pairing by using the first sub-harmonic frequency of the primary roll-up) and a low-frequency forcing Strouhal number $Str_2 = f_2 h/U_\infty = 0.08$ (to influence the behaviour of the entire separation bubble). In addition, we had information from corresponding experiments by Siller and Fernholz [30] that there is an optimum Strouhal number, $Str_{opt} = 0.08$, for a maximum reduction of the mean re-attachment length at a higher Reynolds number, $Re_h = 10500$. For our manipulated flow case ($Re = 3000$) we have chosen an amplitude of $A = 0.5$ which is lower than the amplitude ($A = 2.2$) chosen in the experiments. The higher the forcing amplitude the more difficult and costly are the numerical simulations. Therefore, no attempt has been made for this flow case to systematically vary the forcing amplitude. This can be done much more efficiently in the experiment; see a compilation of relevant data in Siller [31].

3. Discussion of results and comparison with experimental data

3.1. The non-manipulated flow ($Re_h = 3000$)

In *figure 4* we compare the mean flow and the second-order statistics from the two simulations and, in addition, with available experimental data from Larsen [29]. The results for the mean flow field show that a nearly grid independent solution has been provided for the first-order statistics. However, the results for the second-order statistics show larger quantitative differences indicating insufficient spatial resolution in the coarse-grid DNS. In general, the coarse-grid results are below the fine-grid results with the exception of the results in the outer flow region ($Z > 2.5$) and the result for the Reynolds stress, $-\langle uw \rangle$, in the re-attachment region (around $X = 13.0$) where they are above the fine-grid results. In comparing the DNS results with the available experimental data it must be kept in mind that in the wind tunnel experiment large turbulence intensity was present in the outer flow. In addition, the channel height in the experiment was about 7.5 obstacle heights, and in the numerical simulations we used a vertical extension of the computational domain of 5.0 obstacle heights ($L_z = 5.0$) which causes differences in the mean flow field. In the following we consider the fine-grid DNS as the reference for the validation of the large-eddy simulation (LES) of the same flow problem.

Figure 5 compares the first-order and the second-order statistics of a large-eddy simulation (on a grid with 1.7 million grid points) with the fine-grid DNS (on a grid with 51.6 million grid points). For such a comparison, either the DNS data should be filtered with the grid size used in the LES, or the unfiltered DNS data are compared with the grid scale LES data, with an approximated SGS contribution added. We have chosen the second option for all the figures shown here. The SGS turbulence model used in the LES is the classical Smagorinsky SGS model (with $c_s = 0.1$).

The agreement between the two numerical simulations is surprisingly good, and the deviations are smaller than the differences between the coarse-grid DNS (6 million grid points) and the fine-grid DNS (see *figure 4*). The wall-shear stress distributions for the two cases (LES and reference DNS) are in good agreement and typical measures can be evaluated for the mean separation distance in front of the fence (LES: $x_f/h = 1.9$, DNS: $x_f/h = 2.0$), the mean re-attachment position of the main recirculation zone behind the fence (LES: $x_f/h = 12.8$, DNS: $x_f/h = 13.2$) and the size of a secondary separation zone immediately behind the flow obstacle (LES: $x_f/h = 2.7$, DNS: $x_f/h = 2.6$). A second calculation using the so-called dynamic SGS turbulence model (c_s evaluated as a function of space and time) did not show significantly different results. We

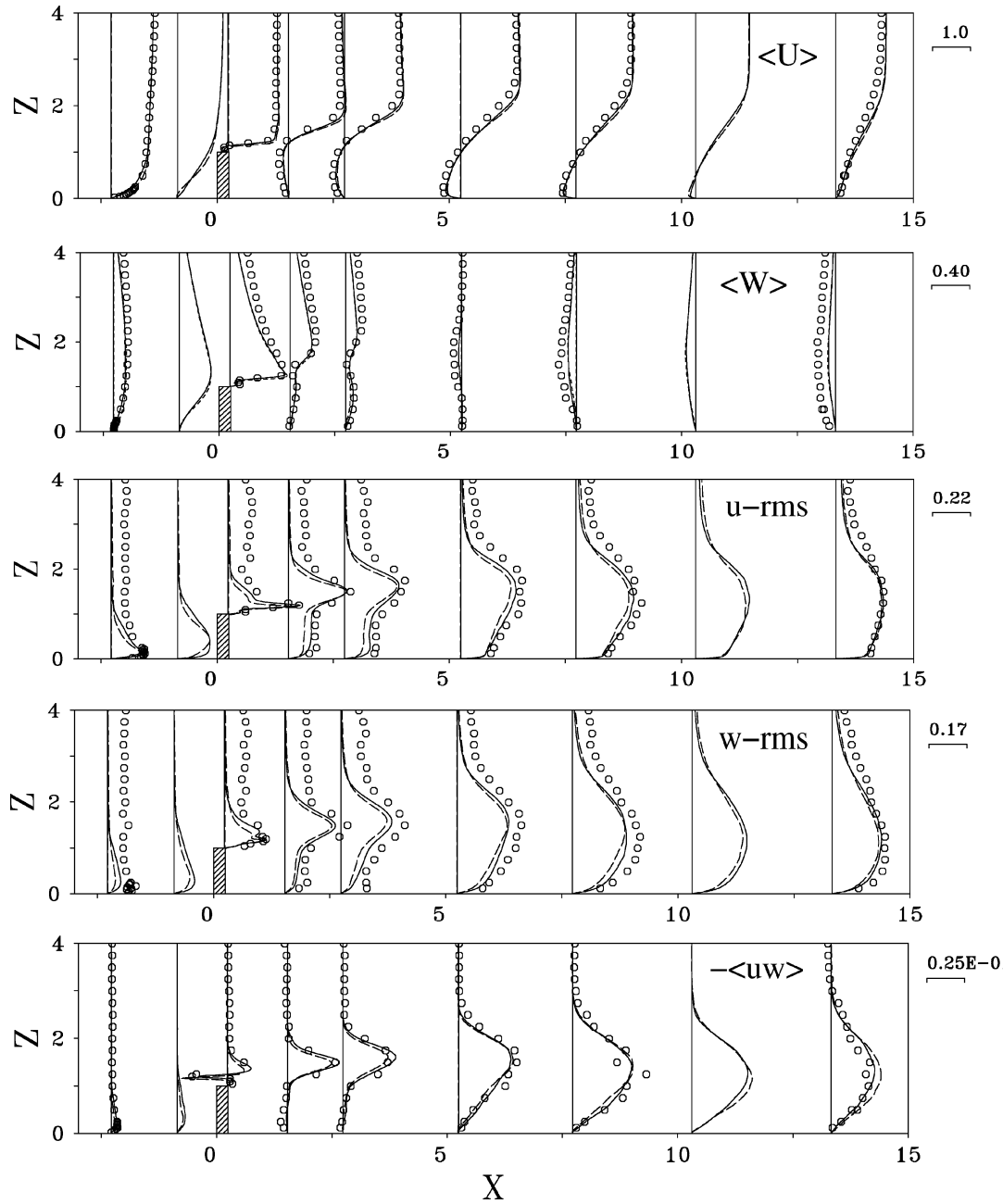

Figure 4. Comparison of fine and coarse grid DNS results with experimental data; (full line) fine grid DNS, (dashed line) coarse grid DNS, (o) experiment.

therefore considered the LES sufficiently validated to carry out the numerical simulations (LES) of turbulent flow over a fence manipulated with two different forcing frequencies ($Str_1 = 0.60$, $Str_2 = 0.08$). The results will be described in section 3.3. In the following section 3.2 we first compare LES results for a higher Reynolds number with available experimental data from Siller and Fernholz [30,31].

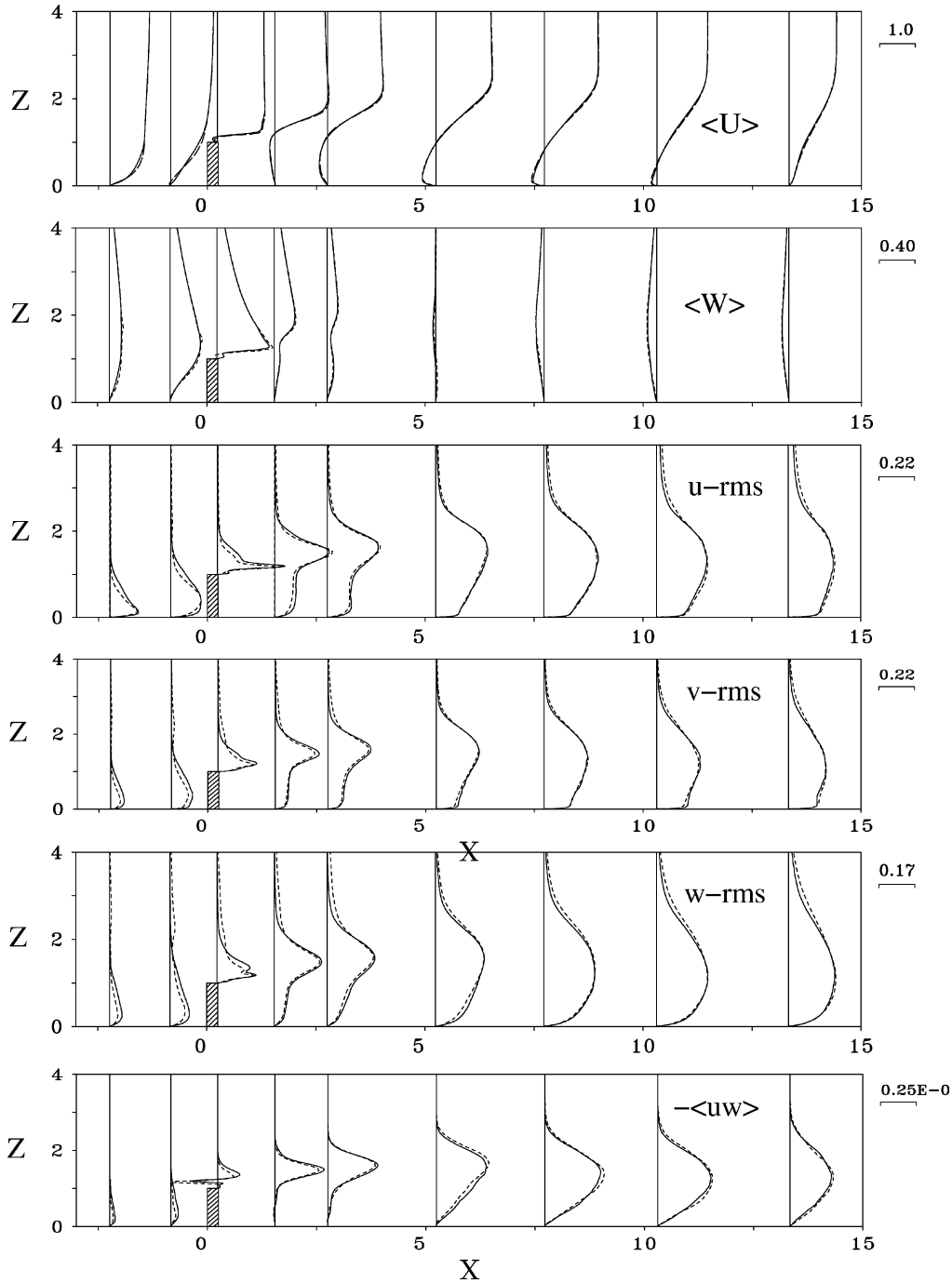

Figure 5. Comparison of LES with DNS results; (full line) fine grid DNS, (dashed line) LES. Note: LES data are the sum of grid scale quantities and approximated sub-grid scale contributions.

3.2. The non-manipulated flow case at higher Reynolds number ($Re_h = 10500$)

In the experiment of Siller and Fernholz [30,31] a peculiar geometry of the fence has been used: the surface-mounted flow obstacle had a top face inclined under 45°, i.e. re-attachment of flow on the (usually flat) top face was avoided. In the numerical simulation we approximated this inclined top face by blocking out corresponding grid cells in a stepwise fashion, see *figure 6*. However, as long as the thickness, t, of the fence is small in comparison with its height, h, (here $t/h = 0.25$) there is no significant effect on the results. *Figure 7* compares the results for the mean wall-skin friction coefficient. The locations of zero wall-shear stress (equivalent to locations of changes in sign of the mean streamwise velocity close to the wall and to the locations of a reverse-flow factor of 50%) signalize the size of the mean separation zone in front of the fence (LES: $x_f/h = 0.55$, experiment: $x_f/h = 0.65$), the mean recirculation zone behind the flow obstacle (LES: $x_r/h = 13.45$, experiment: $x_r/h = 13.6$) and a secondary recirculation zone immediately after the fence (LES: $x_{rs} = 1.55$, experiment: $x_{rs}/h = 1.60$). The time-mean values of the skin-friction coefficients, C_f, from DNS are accurate but their evaluation is very expensive. The coefficients from LES data should also be accurate as

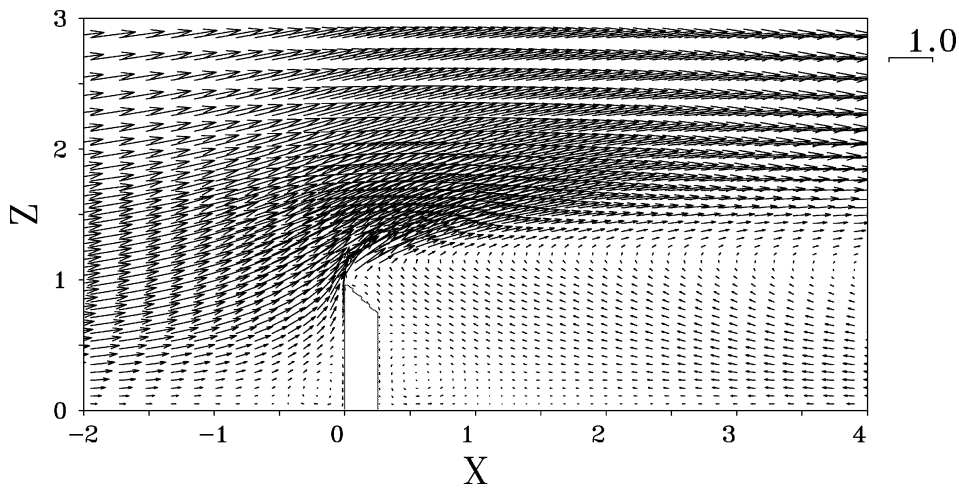

Figure 6. Geometry of fence with a sharp edge of 45° and vector plot of mean flow in a vertical cross-section. Note: vectors shown at every third grid point only.

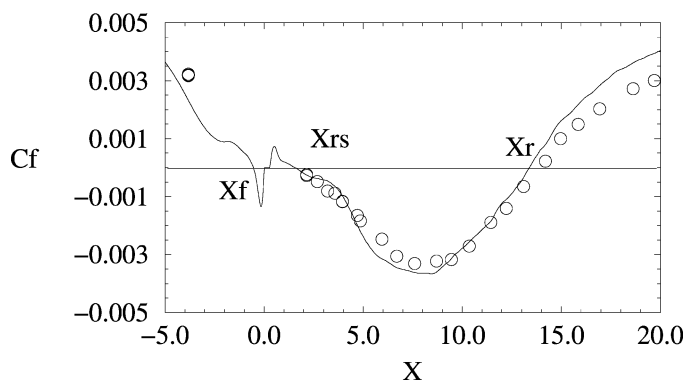

Figure 7. Horizontal profiles of mean wall-skin friction coefficient $C_f = 2\tau_w/(\rho U_\infty{}^2)$; (full line) LES of non-manipulated case, (o) experiment. $X_f = x_f/h$: separation distance in front of the fence; $X_{rs} = x_{rs}/h$: secondary re-attachment length; $X_r = x_r/h$: main re-attachment length.

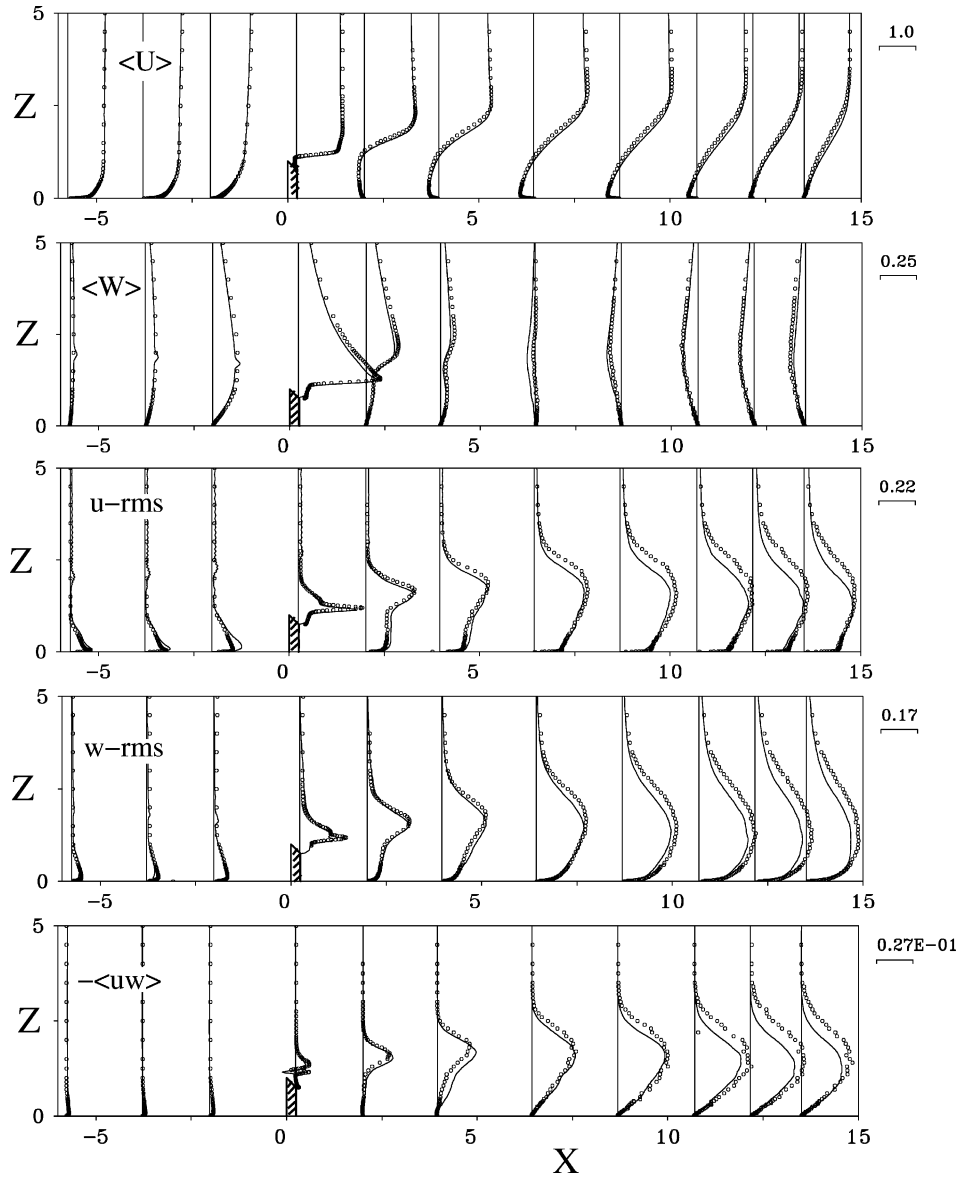

Figure 8. Vertical profiles of mean longitudinal velocity $\langle U \rangle$ for the (non-manipulated) reference case at different positions X, (o) experiment, (full line) LES (sum of grid scale quantities and approximated sub-grid scale contributions).

long as the viscous sublayer is resolved. In our case the first LES grid point is located just at the edge of the viscous sublayer. An evaluation of C_f via the logarithmic law-of-the-wall is not possible because it doesn't exist in the recirculation region and in the relaxation zone after re-attachment. However, the locations of zero wall-shear stress and of changes in sign of the mean streamwise velocity close to the wall and of locations of the 50% reverse-flow factor give reliable measures of mean separation and mean re-attachment lengths. In *figure 8* the first-order and second-order statistics are presented. The mean flow field from LES is in good agreement with the experiment. In front of the fence, only the peak u-rms values deviate noticeably from the experimental data. After the fence, the calculated second-order statistics (grid scale quantities plus approximated sub-grid scale contribution) seems to be systematically below the experiment during its downstream development (at

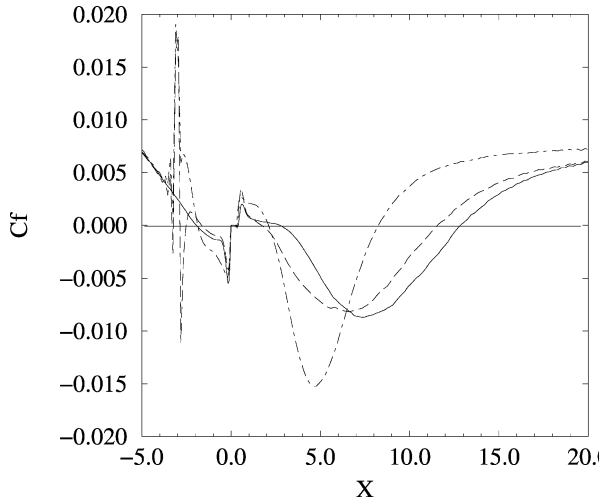

Figure 9. Horizontal profiles of mean wall-skin friction coefficient $C_f = 2\tau_w/(\rho {U_\infty}^2)$; (full line) $Str = 0$, (dashed line) $Str = 0.6$, (dash-dotted line) $Str = 0.08$.

the height of the maximum mean streamwise velocity) in contrast to the results at the low Reynolds number ($Re = 3000$). This could be an indication of stronger convective transport of sub-grid scale turbulence quantities which cannot be represented by the eddy-viscosity SGS model used here. Using the dynamic SGS model mentioned above, or applying a no-slip boundary condition at the upper boundary of the computational domain did not change the results significantly. Therefore, this flow case could be an interesting test case for the development of improved SGS models for higher Reynolds numbers (for example, adding a transport equation for the SGS turbulent energy would provide the missing convective transport mentioned above).

3.3. The manipulated flow cases ($Re_h = 3000$, $Str_1 = 0.60$, $Str_2 = 0.08$)

3.3.1. Mean re-attachment length

In *figure 9* the normalized mean wall shear stress, the wall skin-friction coefficient, $C_f = 2\tau_w/(\rho {U_\infty}^2)$, is shown for the two manipulated flow cases in comparison to the non-manipulated reference case. The mean re-attachment length of the non-manipulated reference case, $x_r/h = 12.8$, is reduced by about 10% to $x_r/h = 11.5$ applying a high-frequency forcing Strouhal number, $Str_1 = 0.60$. A much stronger reduction (36%) to $x_r/h = 8.2$ can be achieved by applying the low-frequency forcing Strouhal number, $Str_2 = 0.08$. There is also a secondary recirculation zone immediately after the fence which decreases from $x_r/h = 2.7$ (non-manipulated case) to $x_r/h = 1.5$ (for $Str_1 = 0.60$) and increases again to to $x_r/h = 2.0$ (for $Str_2 = 0.08$). The negative maximum of the wall skin-friction coefficient changes from about $C_f \approx -0.008$ ($Str = 0.0$ and $Str_1 = 0.60$) by nearly a factor of two to $C_f \approx -0.015$ for the low-frequency forcing ($Str_2 = 0.08$).

3.3.2. First- and second-order statistics

Figure 10 compares the three cases showing selected vertical profiles of the first-order and second-order statistics at the same upstream and downstream location, X. It can be observed that in the low-frequency forcing case ($Str_2 = 0.08$) already the flow in front of the fence is significantly altered. Because of the different mean re-attachment lengths, the three vertical profiles do not belong to equivalent locations. Therefore, in *figure 11* the vertical profiles are redrawn at the same relative location with respect to the mean re-attachment length. *Figure 11* shows that, on the average in time, the high-frequency forcing case is quite similar to the non-

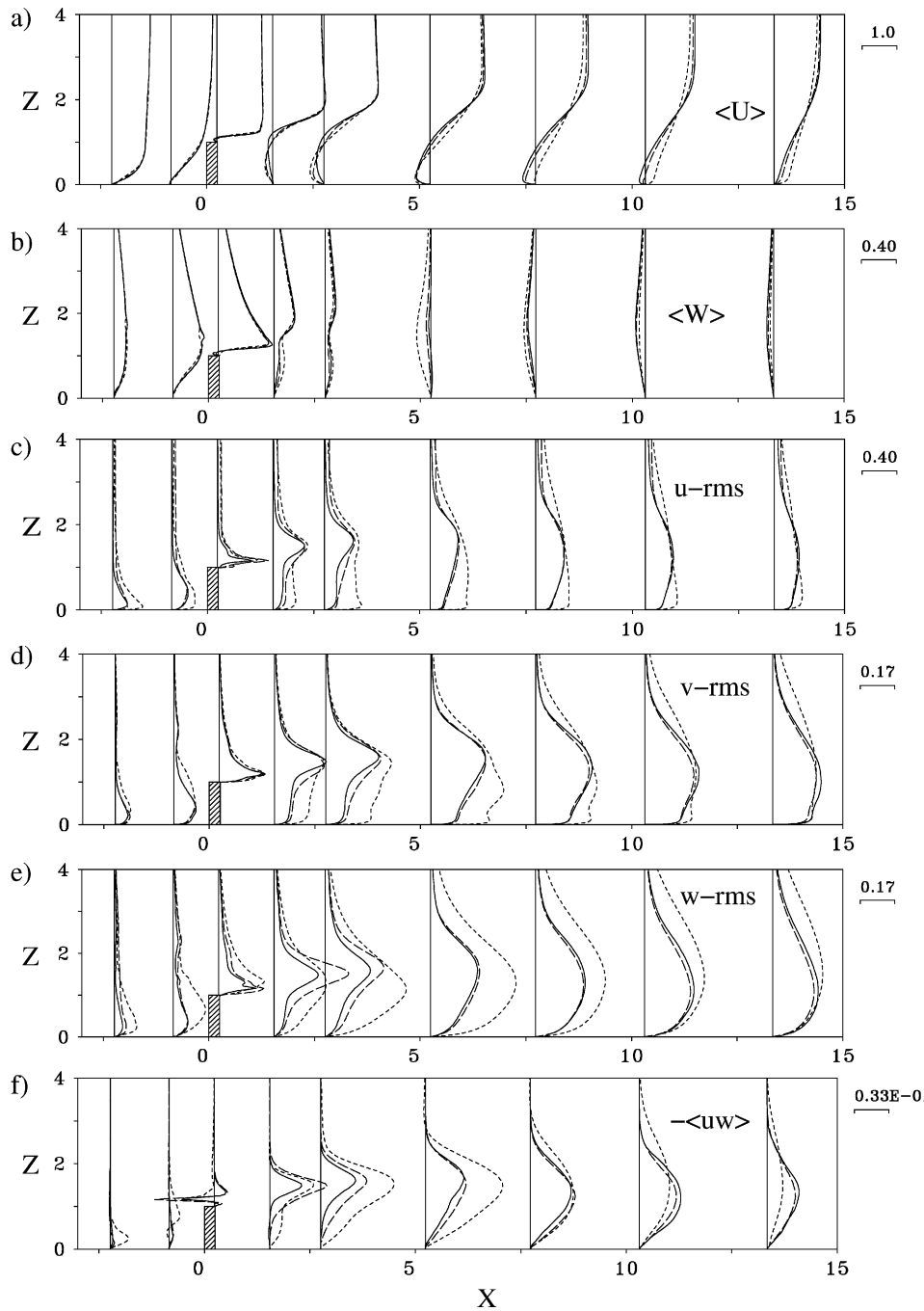

Figure 10. Comparison of vertical profiles at absolute x/h-positions; (full line) $Str = 0$, (long dashes) $Str = 0.6$, (short dashes) $Str = 0.08$.

manipulated reference case, but the low-frequency forcing case ($Str_2 = 0.08$) is significantly different. The mean flow profiles are still qualitatively similar to the other two cases, but the rms profiles are quite different. Much stronger rms-values of the velocity fluctuations in all three coordinate directions are produced. Note, the forcing amplitudes are the same for the two manipulated flow cases and the direct effect of the time-periodic

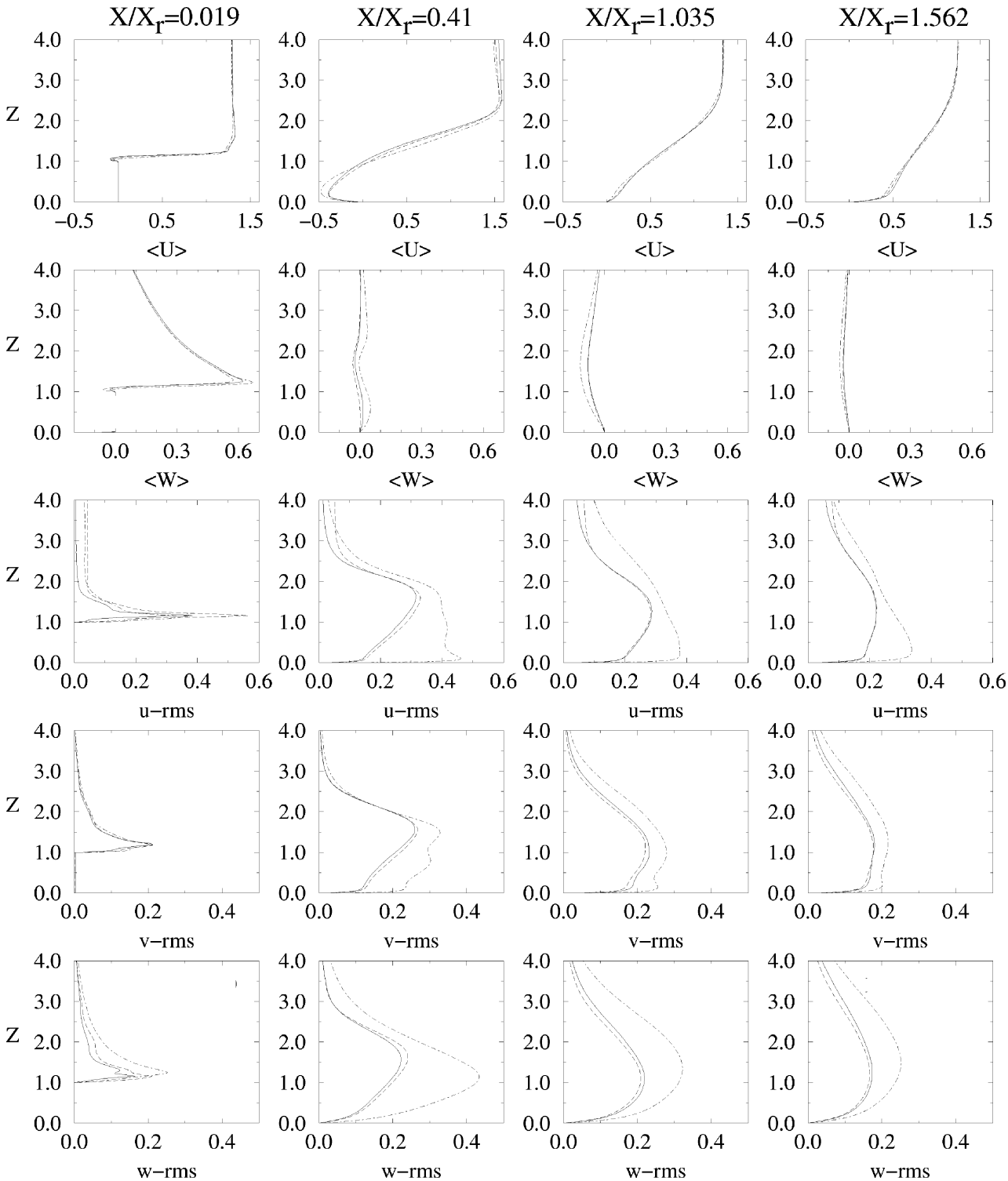

Figure 11. Comparison of vertical profiles at relative x/x_r-positions; (full line) $Str = 0$, (dashed line) $Str = 0.6$, (dash-dotted line) $Str = 0.08$.

blowing/suction manipulation (at $X = -3.0$) is visible in increased rms-values in the outer flow field (say, for $Z > 3.0$), however, this effect is not very strong.

3.3.3. Instantaneous flow fields

Figure 12 shows, on the left column, snapshots from a video of the non-manipulated flow at different equidistant instants of time. For the two other manipulated cases (middle and right column) the snapshots are taken at equal phase angles ($\phi = 0, \pi/2, \pi, (3/2)\pi, 2\pi$) during a complete cycle of the time-periodic forcing. The snapshots show three-dimensional surfaces of equal positive (green) and negative (red) values of the fluctuations of the vertical velocity component, $w'/U_\infty = W' = +/-0.08$.

In the non-manipulated case (left column of *figure 12*) the roll-up process of the shear layer (created at the edge of the flow obstacle) is strongly influenced by the elongated flow structures (streaks) of the incoming turbulent boundary layer. They cause phase distortions in the (basically) two-dimensional roll-up process. In the high-frequency forcing case ($Str_1 = 0.60$) the two-dimensional forcing structure initiates again a stronger two-dimensional roll-up of the separating shear layer, and magnified mixing across this free shear layer (entrainment) causes a shortening of the mean recirculation domain. In the low-frequency forcing case ($Str_2 = 0.08$) large two-dimensional structures are created already in front of the flow obstacle. They roll over the fence (nearly undisturbed by the flow obstacle) and, after the fence, they fill the entire height of the recirculation domain, rolling downstream and thereby entraining a lot of fluid material from outside. As a consequence of this increased exchange with the outer flow the mean recirculation domain is significantly reduced in its length (36%).

3.3.4. Energy spectra

Figure 13 presents an overview of the downstream development of time spectra (of the vertical velocity component, W) along a line at height $Z = 1.287$. The energy ordinate is linear and arbitrarily normalized but the normalization is the same for all three cases. In addition, we present the 2D energy surfaces from two different angles of view.

In the non-manipulated reference case (see *figure 13(a)*) there is no dominant peak visible after separation ($X > 0$). With increasing downstream distance, low frequencies are amplified. In the manipulated flow cases (both with distortion amplitude $A = 0.5$) most of the energy is contained in the forcing frequencies ($Str_1 = 0.6$) and ($Str_2 = 0.08$) over a relatively short downstream distance. In the high-frequency forcing case the energy for $Str = 0.6$ is first amplified and then damped again. In this case the fundamental roll-up with $Str = 1.2$ is visible as a second peak (see *figure 13(b)*). An earlier and stronger amplification of low frequencies (in comparison to the reference case) with increasing downstream distance can be observed. In the low-frequency forcing case (see *figure 13(c)*) the energy for the forcing frequency $Str_2 = 0.08$ is first damped over a short distance and then strongly amplified during the entire downstream development.

More detailed information can be obtained from *figure 14* showing selected time-spectra for three typical regions of the flow: upstream of the fence (X X X), immediately at and shortly after separation (* * *), before re-attachment, at re-attachment and further downstream (+ + +). Note, the range of the Strouhal number shown in *figure 14* is smaller than actually used in the evaluation of the time records. Every twentieth time step of the numerical simulation a sample was taken for the evaluation of the Fourier analysis. This leads to a cut-off of $Str = 6.25$, see *figure 15* (the corresponding cut-off of the LES was at the much higher dimensionless frequency $Str = 125.0$). In the non-manipulated case (see *figure 14(a)*, uppermost row of spectra) the flow domain in front of the obstacle (X X X) shows spectra which reflect the properties of the incoming boundary layer, in particular at the location $X = -2.1$. The spectra at the other two locations closer to the fence seem to be influenced by processes related to the shear layer bounding the separation region in front of the fence, i.e. low frequency

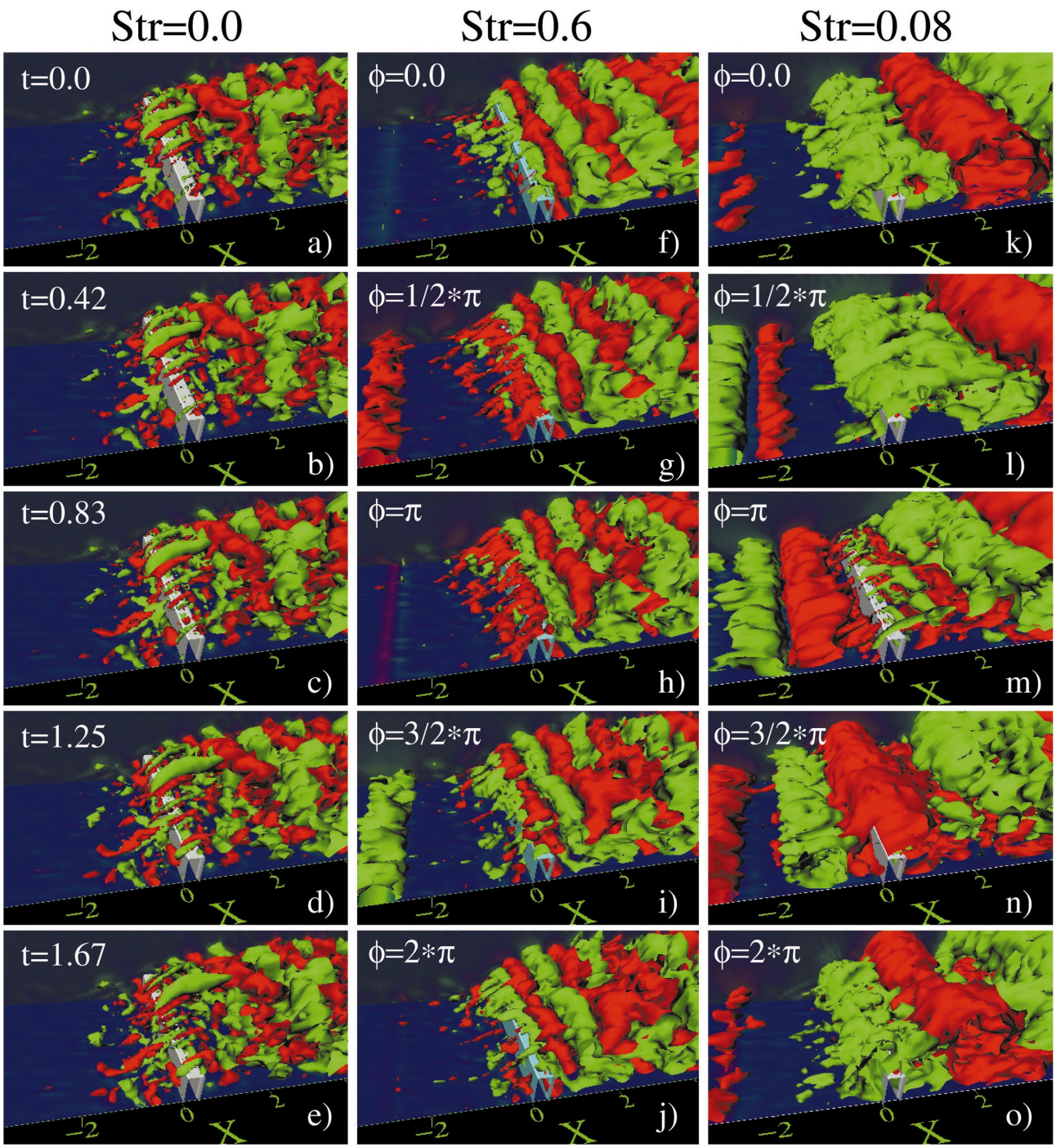

Figure 12. Instantaneous flow structures of non-manipulated and manipulated flow cases ($Str = 0.60$ and $Str = 0.08$): left column: non-manipulated case at equidistant instants of time, middle and right column: manipulated cases at equidistant phase angles ($\phi = 0, \pi/2, \pi, (3/2)\pi, 2\pi$), during a full cycle of the time-periodic forcing. Surfaces of constant dimensionless vertical velocity fluctuation: $W' = +0.08$ (green) and $W' = -0.08$ (red).

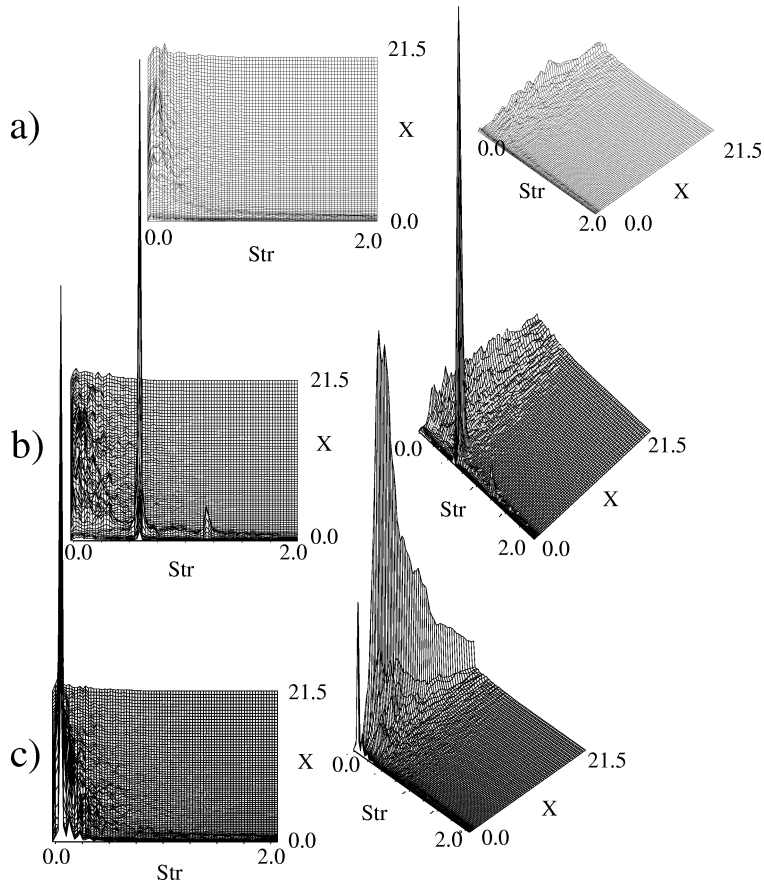

Figure 13. Downstream development of energy spectra in a horizontal plane at ($Z = 1.287$): above: non-manipulated case, middle: manipulated case with $Str = 0.60$, below: manipulated case with $Str = 0.08$.

processes are amplified. The flow region at and after separation (* * * *) shows at $X = 0.6$ an amplification of frequencies in the range ($0.3 < Str < 1.8$) with a peak at $Str = 1.2$ (in our case the fundamental frequency of the primary roll-up of the shear layer). To demonstrate that at $X = 0.6$ there is no accumulation of energy at higher frequencies we present this spectrum again in *figure 15* on extended scales for the energy and for the Strouhal number. Between $X = 0.6$ and $X = 2.0$ energy is transferred to lower frequencies, first to $Str = 0.6$ and then to $Str = 0.3$, signalizing two pairing events in the shear layer. Around re-attachment ($X = 13.0$) most of the energy is contained in the low frequencies. Further downstream ($X \approx 20.0$) there is a peak visible at $Str = 0.08$ (in all three flow cases). In the high-frequency forcing case (see *figure 14(b)*, middle row of spectra) the flow in front of the fence (X X X) is characterized by the forcing frequency and, in addition, by increased levels of energy for all frequencies. After separation (* * * *) the spectra between $X = 1.0$ and $X = 2.0$ only exhibit peaks at the fundamental frequency, $Str = 1.2$, in addition to the peaks at the (sub-harmonic) forcing frequency, $Str = 0.6$. Around and after re-attachment (+ + +) the spectra are quite similar to those of the non-manipulated case. In the low-frequency forcing case (see *figure 14(c)*, bottom row of spectra) all the spectra are dominated by the low-frequency forcing with $Str = 0.08$, and its higher harmonics also contain large amounts of energy. The flow around and after re-attachment is dominated by large structures with a typical frequency $Str = Str_2 = 0.08$. This is also the case in the two other flows but in this case the energy of these structures is significantly amplified. In all three flow cases these large-scale structures leave the separation zone behind

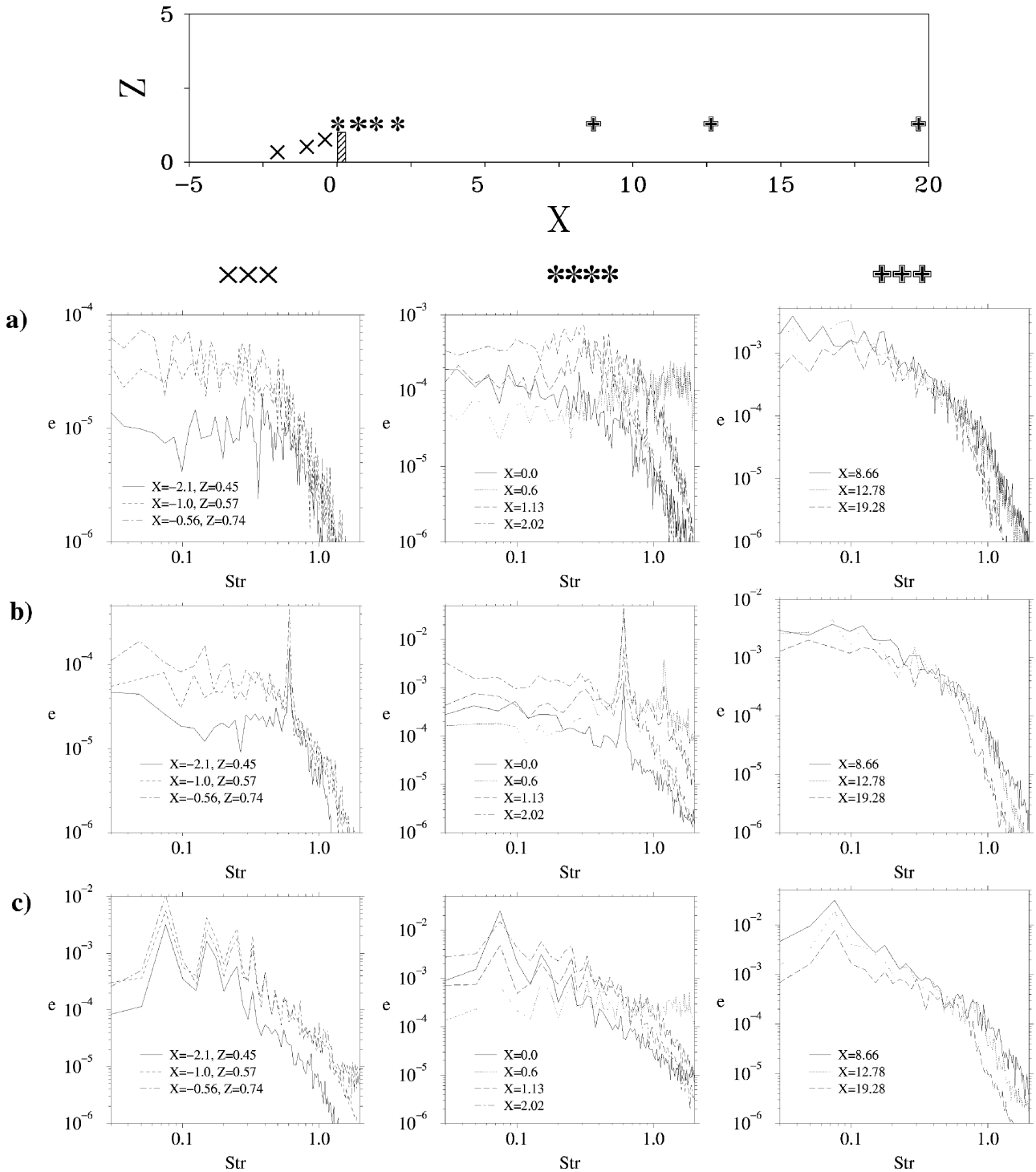

Figure 14. Energy spectra at selected locations in typical flow regions of (a) the non-manipulated case and the manipulated cases ((b) $Str = 0.60$ and (c) $Str = 0.08$): left column (XXX): flow region in front of fence, middle column (****): flow region at and after separation ($Z = 1.287$), right column (+++): flow region before, at and after reattachment ($Z = 1.287$). Note, this figure does not show the total range of Strouhal numbers used in the evaluation of the spectra, see *figure 15*.

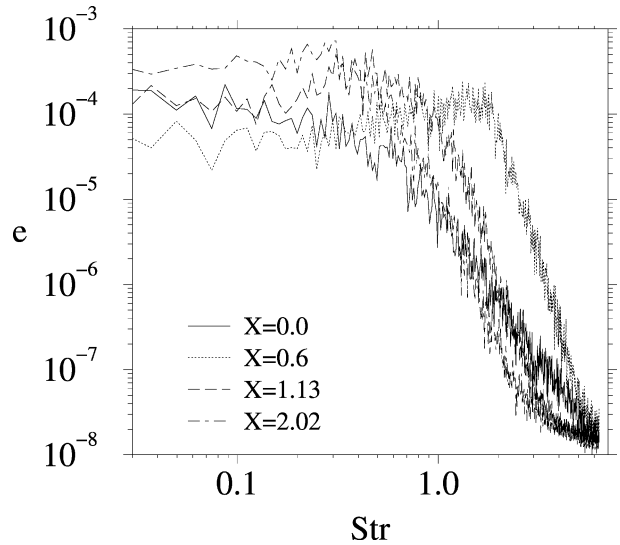

Figure 15. Energy spectrum at ($X = 0.6$, $Z = 1.287$) of the non-manipulated case showing the total range of Strouhal numbers used in the evaluation of all spectra.

the flow obstacle and they are the first dominant structures in the newly developing turbulent boundary layer. Looking back to the results (+ + +) of the case without forcing in *figure 14(a)* this typical low frequency Strouhal number ($Str = 0.08$) can be recognized from the spectrum at $X = 19.28$, and from zoomed views of the complete 2D surfaces of the spectra in *figure 13(a)* (we also had this type of information at different heights). Nevertheless, to get a better resolution at low frequencies, longer time records from the numerical simulation should be evaluated. The experimental data of Siller [31] for the unforced case ($Re = 10500$) show a clear peak around 20 Hz, corresponding to a Strouhal number of $Str \approx 0.08$.

3.3.5. Two-point correlations and integral length scales

Finally, in *figure 16*, showing the spatial correlation coefficients of the vertical velocity component, $R_{ww}(x, \Delta x, z) = \langle w(x, y, z, t)w(x + \Delta x, y, z, t)\rangle / w^2_{rms}$, integral length scales, $L^x_{ww} = \int R_{ww}\, dx$, have been marked at selected locations of the flow field. (Note, for simplicity the closest zero-crossings of the functions R_{ww} have been taken as the limits for the integration.) Close to the edge of the fence, at $(X, Z) = (0.6, 1.16)$, the case with low-frequency forcing ($Str_2 = 0.08$) exhibits nearly a doubling of the integral length scale in comparison to the two other cases ($Str = 0$, $St_1 = 0.6$), see *figure 16(a)*. Further downstream, at $(X, Z) = (3.0, 1.16)$, see *figure 16(b)*, the integral length scales are again doubled in all three flow cases, indicating pairing processes in the shear layer. At a still further downstream position, at $(X, Z) = (13.0, 1.16)$, see *figure 16(c)*, the integral length scales are again enlarged and closer to each other. The most striking feature is exhibited by the low-frequency forcing case ($Str_2 = 0.08$): the entire flow field is dominated by length scales significantly larger than in the other cases.

4. Conclusions

Direct numerical simulation (DNS) of turbulent flow over a surface-mounted fence has been carried out for a Reynolds number of $Re_h = 3000$ to provide a reference data set for the validation of a corresponding large-eddy simulation, using much less grid points than the DNS and requiring about 4% only of the DNS computing

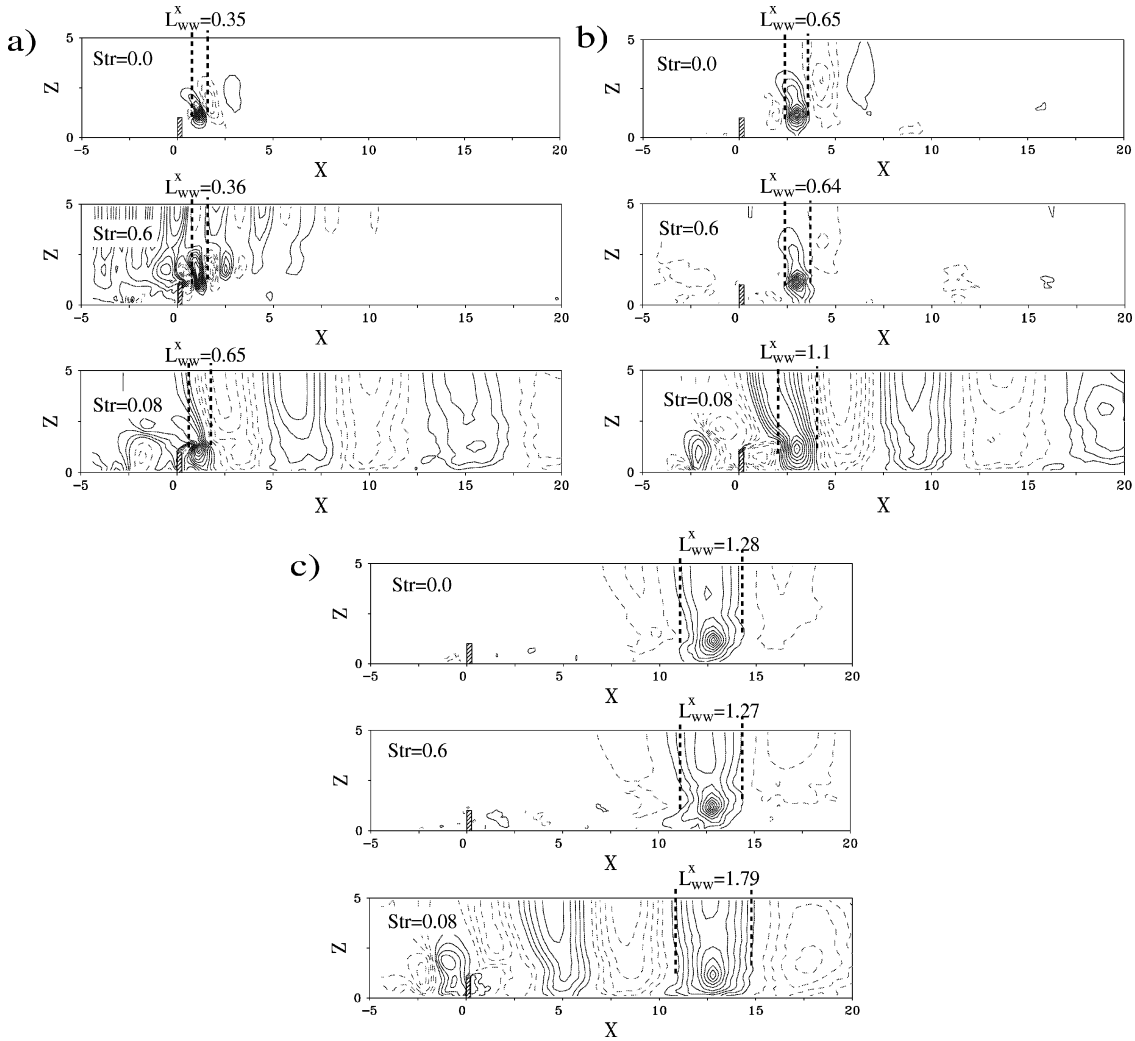

Figure 16. Two-point spatial correlation coefficients, $R_{ww}(x, \Delta x, z) = \langle w(x, y, z, t)w(x + \Delta x, y, z, t)\rangle / w^2_{rms}$, and integral length scales, $L^x_{ww} = \int R_{ww}\, dx$, for the vertical velocity component in three selected downstream locations: (a) $(X, Z) = (0.6, 1.16)$, (b) $(X, Z) = (3.0, 1.16)$, (c) $(X, Z) = (13.0, 1.16)$, for the non-manipulated flow case ($Str = 0$), for the high-frequency forced flow case ($Str_1 = 0.6$) and for the low-frequency forced flow case ($Str_2 = 0.08$).

time. In addition, two manipulated flow cases were investigated with the purpose of controlling the size of the mean separation zone behind the flow obstacle by time-periodic blowing/suction disturbances through a narrow cross-wind slot located three fence heights upstream of the flow obstacle. Two forcing frequencies have been selected: in the first case, $Str_1 = f_1 h/U_\infty = 0.60$, to influence the separated shear layer during its roll-up and pairing phase and, in the second case, $Str_2 = f_2 h/U_\infty = 0.08$, to affect the behaviour of the entire separation bubble. Using the high-frequency forcing Strouhal number ($Str_1 = 0.60$) the mean re-attachment length was reduced by 10% in comparison to the non-manipulated reference case. Using the low-frequency forcing Strouhal number ($Str_2 = 0.08$) a much stronger reduction of 36% could be achieved. The most striking feature is exhibited by this low-frequency forcing case: large-scale structures are already created in front of the flow obstacle, they roll over the fence (nearly undisturbed) and they fill out the entire height of the separation zone behind the fence. As a major conclusion, and in agreement with corresponding experiments by Siller and

Fernholz [30] at a higher Reynolds number ($Re_h = 10500$), the optimum forcing Strouhal number seems to be related to the typical low-frequency movement of the entire separation bubble and not to the instability mode of the separating shear layer.

Many fruitful discussions and exchanges of data with the experimental research group of Professor H.H. Fernholz at the Hermann-Föttinger-Institut (TU Berlin) have led to invaluable insights. There is a complementary nature involved in experimental and numerical simulation investigations. In our flow case, the main advantage on the experimental side was the efficiency and the relative easiness with which different parameters could be tested. On the other hand, the numerical simulation, in particular DNS, is capable to provide spatio-temporal details of the flow which could not be so easily obtained in the experiment.

Acknowledgments

This research was supported by the Deutsche Forschungsgemeinschaft (DFG) under grant number We 705/4+6. We also gratefully acknowledge the support by the Leibniz Computing Center (LRZ) of the Bavarian Academy of Sciences, and by the computing center of the Federal Armed Forces University Munich.

References

[1] Moin P., Mahesh K., Direct numerical simulation: a tool in turbulence research, Annu. Rev. Fluid Mech. 30 (1998) 539–5378.
[2] Eaton J.K., Johnston J.P., A review of research on subsonic turbulent flow reattachment, AIAA J. 19 (1981) 1093–1100.
[3] Adams E.W., Johnston J.P., Effects of the separating shear layer on the reattachment flow structure. Part 1: pressure and turbulence quantities, Exp. Fluids 6 (1988) 400–408.
[4] Adams E.W., Johnston J.P., Effects of the separating shear layer on the reattachment flow structure. Part 2: reattachment length and wall shear stress, Exp. Fluids 6 (1988) 493–499.
[5] Ho C.M., Huerre P., Perturbed free shear layers, Annu. Rev. Fluid Mech. 16 (1984) 365–424.
[6] Liu J.T.C., Coherent structures in transitional and turbulent free shear flows, Annu. Rev. Fluid Mech. 21 (1989) 285–315.
[7] Bushnell D.M., McGinley C., Turbulence control in wall flows, Annu. Rev. Fluid Mech. 21 (1989) 1–20.
[8] Fiedler H.E., Fernholz H.H., On management and control of turbulent shear flows, Prog. Aerospace Sci. 27 (1990) 305–387.
[9] Gad-el Hak M., Interactive control of turbulent boundary layers: a futuristic look, AIAA J. 32 (1994) 1753–1765.
[10] Lumley J., Blossey P., Control of turbulence, Annu. Rev. Fluid Mech. 30 (1998) 311–327.
[11] Gad-el Hak M., Pollard A., Bonnet J.-P. (Eds), Flow Control: Fundamentals and Practices, Lecture Notes in Physics, Vol. 53, Springer-Verlag, Berlin, 1998.
[12] Le H., Moin P., Kim J., Direct numerical simulation of turbulent flow over a backward-facing step, J. Fluid Mech. 330 (1997) 349–374.
[13] Akselvoll K., Moin P., Large eddy simulation of a backward facing step flow, in: Rodi W., Martelli F. (Eds), Proceedings of Engineering Turbulence Modelling and Experiments 2, Elsevier Science Publishers, 1993, pp. 303–313.
[14] Jovic S., Driver D.M., Backward-facing step measurement at low Reynolds number, $Re = 5000$, NASA Tech. Mem 108807, 1994.
[15] Hasan M.A.Z., The flow over a backward-facing step under controlled disturbation: laminar separation, J. Fluid Mech. 238 (1992) 73–96.
[16] Hasan M.A.Z., Khan A.S., On the stability characteristics of a reattaching shear layer with nonlaminar separation, Int. J. Heat Fluid Fl. 13 (1992) 224–231.
[17] Chun K.B., Sung H.J., Control of turbulent separated flow over a backward-facing step by local forcing, Exp. Fluids 21 (1996) 417–426.
[18] Chun K.B., Sung H.J., Response of separated flows over a backward-facing step to local forcing, 11th Symposium on Turbulent Shear Flows, September 8–11, Grenoble, France, 1997, pp. 26/13–26/17.
[19] Huppertz A., Janke G., Preliminary experiments on the control of three-dimensional modes in the flow over a backward-facing step, in: Machiels L., Gavrilakis S., Monkewitz P.A. (Eds), Advances in Turbulence VI, Kluwer Academic Publishers, 1996, pp. 461–464.
[20] Wengle H., Bärwolff G., Janke G., Huppertz A., The manipulated transitional backward-facing step flow: an experimental and direct numerical simulation investigation, Eur. J. Mech. B-Fluids (2000) (accepted for publication).
[21] Good M.C., Joubert P.N., The form drag of two-dimensional bluff-plates immersed in turbulent boundary layers, J. Fluid Mech. 31 (1968) 547–582.
[22] Ruderich R., Fernholz H.H., An experimental investigation of a turbulent shear flow with separation, reverse flow, and reattachment, J. Fluid Mech. 163 (1986) 283–322.
[23] Castro I.P., Haque A., The structure of a shear layer bounding a separation region. Part 2: effects of free-stream turbulence, J. Fluid Mech. 192 (1988) 577–595.

[24] Kelso R.M., Lim T.T., Perry A.E., The effect of forcing on the time-averaged structure of the flow past a surface-mounted bluff plate, J. Wind Eng. Ind. Aerod. 49 (1993) 217–226.
[25] Miau J.J., Lee K.C., Chen M.H., Chou J.H., Control of separated flow by a two-dimensional oscillating fence, AIAA J. 29 (1991) 1140–1148.
[26] Kiya M., Shimizu M., Mochizuki O., Sinusoidal forcing of a turbulent separation bubble, J. Fluid Mech. 342 (1997) 119–139.
[27] Sigurdson L.W., The structure and control of a turbulent reattaching flow, J. Fluid Mech. 298 (1995) 139–165.
[28] Weickgenannt A., Monkewitz P., Control of vortex shedding from a blunt cylinder aligned with the flow, Eur. J. Mech. B/Fluids 19 (4) (2000).
[29] Larsen P.S., Database on tc-2c and tc-2d fence-on-wall and obstacle-on-wall test cases, Report AFM-ETMA 95-01, ISSN 0590-8809, TU Denmark, 1995.
[30] Siller H.A., Fernholz H.H., Control of the separated flow downstream of a two-dimensional fence by low-frequency forcing, Appl. Sci. Res. 57 (1997) 309–318.
[31] Siller H.A., Reduction of the recirculation length downstream of a fence by an oscillating cross-flow, PhD thesis, Technische Universität Berlin, Berlin, Germany, 1999.
[32] Rogallo R.S., Moin P., Numerical simulation of turbulent flows, Annu. Rev. Fluid Mech. 16 (1984) 99–137.
[33] Schumann U., Subgrid scale model for finite difference simulations of turbulent flows in plane channels and annuli, J. Comp. Phys. 18 (1975) 376–404.
[34] Ciofalo M., Large-eddy simulation: a critical survey of models and applications, Academic Press, 1994, pp. 321–419.
[35] Fureby C., Towards large eddy simulations of flows in complex geometries, AIAA-98-2806, 1998, pp. 1–17.
[36] Hirt C.W., Nichols B.D., Romero N.C., Sola – a numerical solution algorithm for transient fluid flows, in: Los Alamos Sci. Lab. Report LA 5852, Los Alamos, 1975.
[37] Gresho P.M., Lee R., Don't suppress the wiggles – they're telling you something, Comput. Fluids 9 (1981) 223–253.
[38] Schäfer M.,Turek S., Benchmark computations of laminar flow around a cylinder, Notes on Numerical Fluid Mechanics, Vieweg, Vol. 52, 1996, pp. 547–566.
[39] Manhart M., Zonal direct numerical simulation of turbulent plane channel flow, in: Friedrich R., Bontoux P. (Eds), Proceedings of the 5th French–German Workshop on 'Computation and Visualization of Three-Dimensional Vortical and Turbulent Flows', 6–7 December 1996, Munich University of Technology, Notes on Numerical Fluid Mechanics, Vieweg, Vol. 64, 1998, pp. 51–63.
[40] Kim J., Moin P., Moser R., Turbulence statistics in fully developed channel flow at low Reynolds number, J. Fluid Mech. 177 (1987) 133–166.
[41] Meri A., Wengle H., Dejoan A., Vedy E., Schiestel R., Applications of a 4th-order Hermitian scheme for non-equidistant grids to LES and DNS of incompressible fluid flow, in: Hirschel E.H. (Ed.), Numerical Flow Simulation I, Notes on Numerical Fluid Mechanics, Vieweg, Vol. 66, 1998, pp. 365–381.
[42] Manhart M., Deng G.B., Hüttl T.J., Tremblay F., Segal A., Friedrich R., Piquet J., Wesseling P., The minimal turbulent flow unit as a test case for three different computer codes, in: Hirschel E.H. (Ed.), Numerical Flow Simulation I, Notes on Numerical Fluid Mechanics, Vieweg, Vol. 66, 1998, pp. 365–381.
[43] Jimenez J., Moin P., The minimal flow unit in near-wall turbulence, J. Fluid Mech. 255 (1991) 213–240.
[44] Rodi W., Ferziger J.H., Breuer M., Pourquie M., Status of large eddy simulation: results of a workshop, T. ASME J. Fluids Eng. 119 (1997) 248–262.
[45] Martinuzzi R., Tropea C., The flow around surface-mounted, prismatic obstacles placed in a fully developed channel flow, T. ASME J. Fluids Eng. 115 (1993) 85–92.
[46] Manhart M., Vortex shedding from a hemisphere in a turbulent boundary layer, Theor. Comput. Fluid Dynam. 12 (1998) 1–28.